



# Tectono-magmatic controls on decratonic gold deposits

Jia Chang<sup>1,2</sup> · Andreas Audétat<sup>2</sup> · Jian-Wei Li<sup>1</sup>

Received: 29 November 2020 / Accepted: 4 August 2021 / Published online: 21 August 2021  
© The Author(s) 2021

## Abstract

Magmatic-hydrothermal gold–copper deposits in post-subduction settings represent essential targets for mineral exploration, but controls on their formation remain controversial. The early Cretaceous lode Au districts that formed during lithosphere destruction of the North China Craton provide an ideal opportunity to better understand the key tectono-magmatic factors responsible for the genesis of Au-rich deposits in post-subduction settings. Here, we present a LA-ICP-MS study of silicate melt inclusions and sulfide inclusions from ore-related mafic to intermediate rocks in the central Taihangshan Au district in the interior of the North China Craton to constrain the content and evolution of magmatic ore metals  $\pm$  volatiles. The results, combined with numerical modeling, suggest that the ore-related magmas contained only a few ng/g Au, which is similar to the Au content of non-mineralization-related mafic to intermediate magmas worldwide. The low Au content of the lode Au-related magmas suggest that large volumes of magmas had to accumulate in the middle to lower crust through trans-lithospheric fault systems to produce the lode Au deposits. It is further suggested that the lode Au-related magmas were alkali-rich, hydrous, oxidized and relatively rich in sulfur and chlorine (mafic melt inclusions contain 0.14–0.24 wt% S and 0.1–0.2 wt% Cl). These properties are considered critical for the generation of auriferous ore fluids. By comparing the tectono-magmatic setting of the giant Jiaodong Au province (~4000 t Au) with the central Taihangshan district (~150 t Au), we propose that the much larger total Au tonnage of the Jiaodong district results from the accumulation of a much larger volume of ore-forming magmas at deep crustal levels, induced by a stronger degree of lithosphere modification. In addition, given that the composition of lode Au-related magmas is similar to that of porphyry Cu–Au-related magmas, the lack of giant, early Cretaceous porphyry Cu–Au deposits in the North China Craton suggests that strong extensional settings favor the formation of lode Au deposits instead of porphyry Cu–Au deposits. The present study, therefore, has general implications for the genesis of Au-rich deposits in strongly extensional settings.

**Keywords** Lode Au deposits · LA-ICP-MS · Sulfide inclusions · Melt inclusions · Extensional settings · Craton destruction

## Introduction

Magmatic-hydrothermal ore deposits emplaced in the shallow continental crust host many of the world's largest Cu and Au accumulations (Richards 2009), including porphyry-, skarn- and high-sulfidation epithermal-type ore

deposits. Compared to subduction settings, where porphyry Cu(–Mo–Au) systems related to calc-alkaline magmas develop (Sillitoe 2010), post-subduction settings generally produce Au-rich deposits associated with more alkaline magmas (Jensen and Barton 2000; Richards 2009). Ore-related magmas in post-subduction settings could be derived from partial melting of metasomatized subcontinental lithosphere mantle (SCLM) and/or from re-melting of juvenile mafic lower crust previously extracted from metasomatized upper mantle (Richards 2009). It is commonly thought that the metasomatized SCLM and/or its partial melts are unusually Au-rich and thus favorable for the formation of large gold provinces (e.g., Muntean et al. 2011; Griffin et al. 2013; Tassara et al. 2017). In contrast, a recent study showed that neither the metasomatized SCLM nor its partial melts are particularly Au-rich (Wang et al. 2020a). However, significant

---

Communicated by Gordon Moore.

---

✉ Jia Chang  
cugchangjia@126.com

<sup>1</sup> School of Earth Resources and State Key Laboratory of Geological Processes and Mineral Resources, China University of Geosciences, Wuhan 430074, China

<sup>2</sup> Present Address: Bavarian Geoinstitute, University of Bayreuth, Universitätsstrasse 30, 95447 Bayreuth, Germany

Au enrichment may occur during the subsequent evolution of these magmas, which depends largely on the type and extent of sulfide fractionation (e.g., Li et al. 2019). Considering that ore-forming magmas are differentiated products of mantle partial melts, it is thus important to understand the behavior of Au during magmatic differentiation.

Gold may become enriched in evolved melts if significant magma differentiation occurs without sulfide saturation. If a magma becomes sulfide-saturated during its evolution, the Au content of the residual melts depends on (i) the timing of sulfide saturation, (ii) the type and amount of saturated sulfides, and (iii) the partitioning coefficient of Au between silicate melts and sulfides at specific  $P$ – $T$ – $fO_2$  conditions (Li and Audétat 2012, 2015; Li et al. 2019). There is growing evidence that arc-related basaltic magmas emplaced in the deep crust reached sulfide saturation relatively early, despite their high oxidation state (Lee et al. 2012; Chiaradia 2014; Matjuschkin et al. 2016; Chang and Audétat 2018; Du and Audétat 2020). These studies seemingly support the hypothesis that sulfide-rich lower crustal cumulates can be a potential source for Au-rich magmas (Richards 2009; Hou et al. 2017), provided that the residual sulfides preferentially incorporated Au rather than Cu. However, recent experimental studies and natural observations suggest that these sulfides consist mainly of monosulfide solid solution (Li and Audétat 2012; Chang and Audétat 2018; Du and Audétat 2020), which phase preferentially scavenges Cu rather than Au.

Several early Cretaceous lode Au districts developed in the eastern half of the North China Craton (NCC) under strong extensional settings induced by lithosphere thinning and destruction (Li et al. 2012). This unique tectonic setting has led Zhu et al. (2015) to term the gold deposits as “decratonic Au deposits”. Many of these lode Au deposits are hosted in amphibolite- to granulite-facies metamorphic rocks of Neo-Archean to Paleoproterozoic ages. Since the Au deposits are much younger than the regional metamorphic events, these deposits are clearly not metamorphic-related orogenic Au deposits like those occurring in cratonic blocks worldwide (Groves et al. 1998). Instead, many studies argue for a genetic link between the gold mineralization and coeval mafic to intermediate magmatism sourced from metasomatized SCLM (e.g., Yang et al. 2003; Cao et al. 2012; Li et al. 2012; Tan et al. 2012; Zhang et al. 2017).

In this paper, we first review the early Cretaceous tectono-magmatic setting of the central Taihangshan district (CTD) and then constrain the content and evolution of ore metals  $\pm$  volatiles in lode Au-related magmas by means of silicate melt inclusions and sulfide inclusions in early Cretaceous mafic to intermediate rocks. The results allow us to develop a tectono-magmatic model for the genesis of the lode Au deposits. On this basis, we discuss potential reasons for contrasting tonnage of total Au reserves in the CTD and

the Jiaodong district and for the general lack of early Cretaceous, giant porphyry Cu–Au deposits in the NCC.

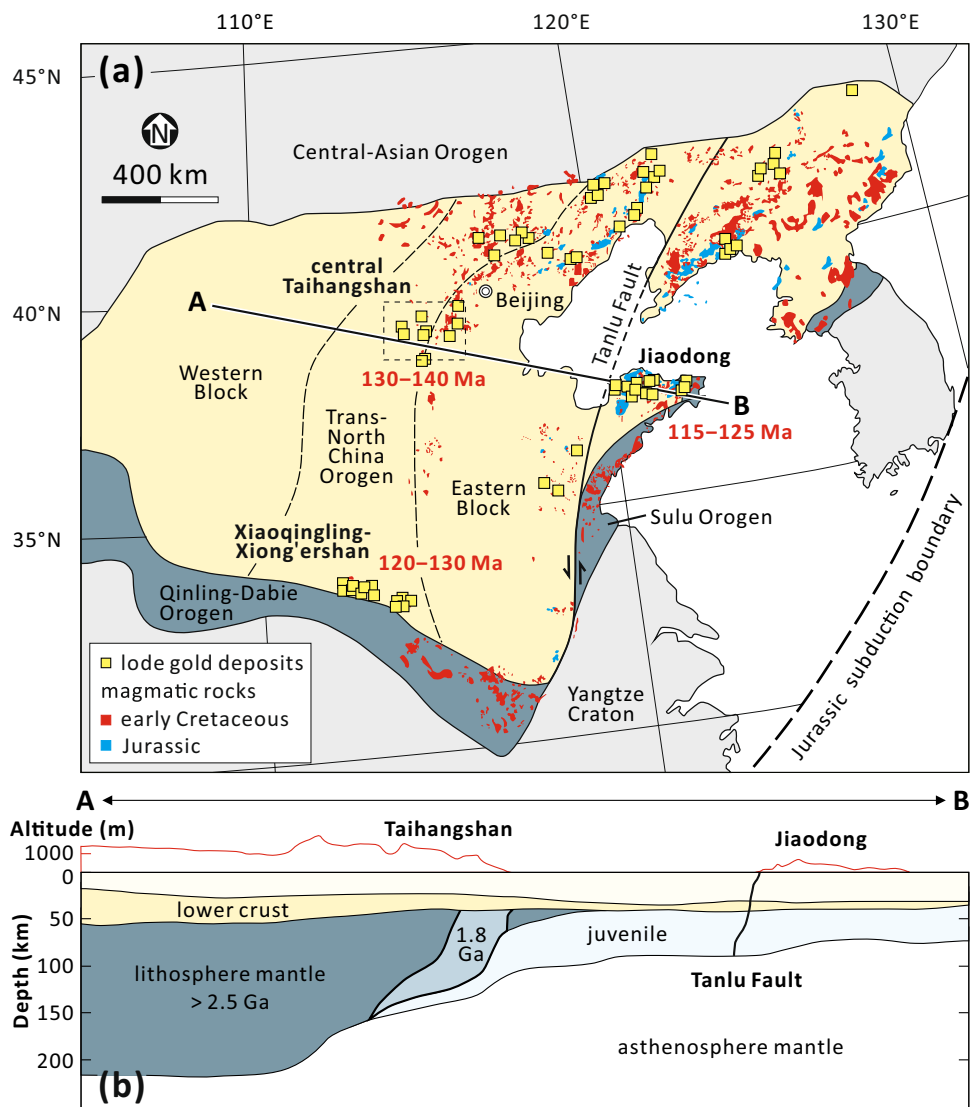
## Geological background

### Geology and early Cretaceous Au mineralization of the NCC

The NCC is located to the north of the Qinling–Dabie–Sulu Orogen and to the south of the Central-Asian Orogen (Fig. 1a). The final amalgamation and stabilization of the NCC is marked by the collision between the Western and Eastern blocks of the craton at  $\sim 1.85$  Ga along the central Trans-North China Orogen (TNCO) (Zhao et al. 2005). The TNCO experienced multiple Neoproterozoic to Paleoproterozoic subduction–accretion–collision events (Tang and Santosh 2018). The basement of the NCC comprises Mesoarchean to early Paleoproterozoic amphibolite to granulite-facies metamorphic rocks (Zhao et al. 2005). From late Paleoproterozoic to late Paleozoic, the NCC remained stable and received continuous deposition of platform carbonate and clastic rocks (Wang and Mo 1995). Subsequently, the southern and northern margins of the NCC were activated by multiple Paleozoic to early Mesozoic orogenic events. The convergence of the Paleo-Asian Ocean from late Permian to Jurassic caused strong magmatism and significant crustal thickening in the northern margin (Xiao et al. 2003). The southern margin was affected by subduction of the Paleo-Tethys slab followed by Triassic collision between the Yangtze Craton and NCC that formed the Qinling–Dabie–Sulu Orogen (Dong et al. 2011). In the late Mesozoic, the eastern portion of the NCC experienced significant thinning or destruction of the ancient lithosphere (Wu et al. 2019), with the lithosphere becoming gradually thinner from the TNCO to the eastern margin of the craton (Fig. 1b). The destruction or thinning of the ancient lithosphere in the NCC culminated during the early Cretaceous, as manifested by widespread early Cretaceous magmatism (Fig. 1a; Zhu et al. 2012; Wu et al. 2019). A younging trend of Jurassic magmatic rocks ( $\sim 145$ – $170$  Ma) from the eastern margin to the central TNCO, and a reverse trend for early Cretaceous magmatic rocks ( $\sim 110$ – $145$  Ma) (Zhang et al. 2014), suggests that the late Mesozoic lithosphere thinning and associated magmatism was triggered by flat subduction and subsequent retreat of the paleo-Pacific slab (Wu et al. 2019). The Sulu segment of the Qinling–Dabie–Sulu Orogen was offset  $\sim 500$  km northward by the sinistral Tan–Lu Fault in the Early Cretaceous (Fig. 1a; Zhu et al. 2010).

The strong lithosphere modification also resulted in the formation of numerous early Cretaceous lode Au deposits in the eastern portion of the NCC, which hosts a total reserve of  $\sim 4000$  metric tons of Au in the Jiaodong district,  $\sim 800$  t

**Fig. 1** **a** Distribution of late Mesozoic magmatic rocks and lode Au deposits in the North China Craton (modified after Wu et al. 2019). Note that the age of Au mineralization shows a younging trend from the central Taihangshan district to the Jiaodong district (data source: Jiaodong district—Zhang et al. 2020; Xiaoqingling–Xiong’ershan district—Li et al. 2012; central Taihangshan district—this study). The dashed-line box marks the study area. **b** Lithospheric thickness across the North China Craton (Zheng et al. 2016). The juvenile lithosphere mantle formed during and/or after the craton destruction in the late Mesozoic



in the Xiaoqingling–Xiong’ershan district, and ~150 t in the central Taihangshan district (Fig. 1a; Yang et al. 2003; Li et al. 2012; Zhu et al. 2015). Large areas along the northern margin of the NCC also host numerous early Cretaceous lode Au deposits that coexist with some Late Jurassic varieties, having a total Au reserve of > 1000 t (Yang et al. 2003). The early Cretaceous lode Au deposits are generally composed of auriferous quartz-sulfide veins variably associated with disseminated ores in the sericitic alteration zones proximal to the veins. Individual veins typically extend for a few hundred meters to up to 3000 m along strike, and tens to a few hundred meters down dip, with an average thickness of 0.2–4 m (Yang et al. 2003; Li et al. 2012). Major orebodies are hosted in brittle to brittle–ductile faults showing reverse or normal displacement of several to a few tens meters, and mineralization preferentially occurs in bends or jogs or at changes in strike and splays. The average ore grade of these deposits generally ranges from 2 to 30 g/t Au.

Sulfide minerals, accounting for 3–20 vol% of the ores, are dominated by pyrite with subordinate amounts of sphalerite, galena and chalcopyrite. Gold generally occurs as native gold and electrum grains either enclosed by sulfide minerals and quartz or in cracks or interstitial to these minerals. Telluride minerals (e.g., petzite, calaverite and sylvanite) sporadically occur in some deposits. Alteration halos along the auriferous quartz veins are generally well developed, with a variable width of 0.1–2 m. Typical alteration minerals include quartz, sericite, K-feldspar, biotite, chlorite, ankerite and calcite, with quartz-sericite ± chlorite alteration assemblages that are closely associated with gold-bearing pyrite being the most abundant.

Remarkably, the lode Au deposits are commonly spatially associated with abundant, contemporaneous SCLM-derived mafic to intermediate dikes (Yang et al. 2003). In many deposits, the auriferous quartz veins and the mafic to intermediate dikes are controlled by similarly oriented, secondary

structures of regional major faults (such as the Guocheng Au deposit; Tan et al. 2012). Previous geological and geochemical studies demonstrated that the gold mineralization is genetically related to the SCLM-derived magmatism (e.g., Yang et al. 2003; Cao et al. 2012; Li et al. 2012; Tan et al. 2012; Zhang et al. 2017). In the most extensively investigated Jiaodong district, dike swarms in lode Au deposits range from very primitive basaltic compositions (up to ~16 wt% MgO), to rhyolitic compositions (only ~0.5 wt% MgO) (see Supplementary Fig. S1). Nevertheless, most of them are evolved basaltic ( $\leq 11$  wt% MgO) to andesitic ( $\geq 3$  wt% MgO) in composition.

### Geology and mineralization of the central Taihangshan district

The CTD in the interior of the NCC is characterized by Neoproterozoic to Paleoproterozoic basement metamorphic rocks that are unconformably covered by Mesoproterozoic to Paleozoic platform carbonates predominantly in the northeast (Fig. 2a). From northwest to southeast, the exposed basement can be divided into the Hengshan, Wutai and Fuping metamorphic complexes (Zhao et al. 2005; Tang and Santosh 2018). The Hengshan complex consists mainly of granitoid gneisses, amphibolites and mafic granulites, supracrustal rocks and TTG gneisses; the Wutai complex comprises granitoid plutons (diorite and TTG suites), metamorphosed volcano-sedimentary rocks and ultramafic rocks; the major rock types of the Fuping complex are TTG

gneisses, supracrustal rocks, augen granitoid gneisses and gneissic granites. During final amalgamation of the NCC at ~1.85 Ga, the Hengshan and Fuping complexes experienced upper amphibolite- to granulite-facies metamorphism, whereas the Wutai complex experienced greenschist- to lower amphibolite-facies metamorphism. Voluminous early Cretaceous volcanic rocks, plutons and batholiths, and numerous dikes and stocks are widely distributed throughout the entire district (Fig. 2a). The volcanic rocks are andesitic, dacitic and rhyolitic in composition; the plutons and batholiths consist of granodiorite, monzogranite, granite, diorite and/or lesser gabbro; the dikes vary from mafic to felsic compositions, and the stocks are of intermediate to felsic compositions. Compiled geochronological data suggest that most of the magmatic rocks in the CTD were emplaced in the period of ~126–145 Ma, except for some minor mafic to intermediate dikes that were emplaced during ~110–125 Ma (Fig. 2b; Table S1). Regional NNE-trending major faults in the eastern portion of the CTD form a characteristic part of the tectonic framework of the TNCO (Figs. 1 and 2a). The abundant NNE- and NW-trending major and secondary faults in the CTD likely regulated the emplacement of the early Cretaceous magmatic rocks (Fig. 2a).

The CTD hosts abundant lode Au, porphyry/skarn Cu(–Mo), porphyry Mo and hydrothermal Pb–Zn(–Ag–Cu) deposits that are intimately associated with the ~126–145 Ma magmatic rocks (Fig. 2). There are about 15 lode Au deposits in the CTD, which share similar characteristics to those in other gold districts of the NCC (Ding et al. 1992; Cao

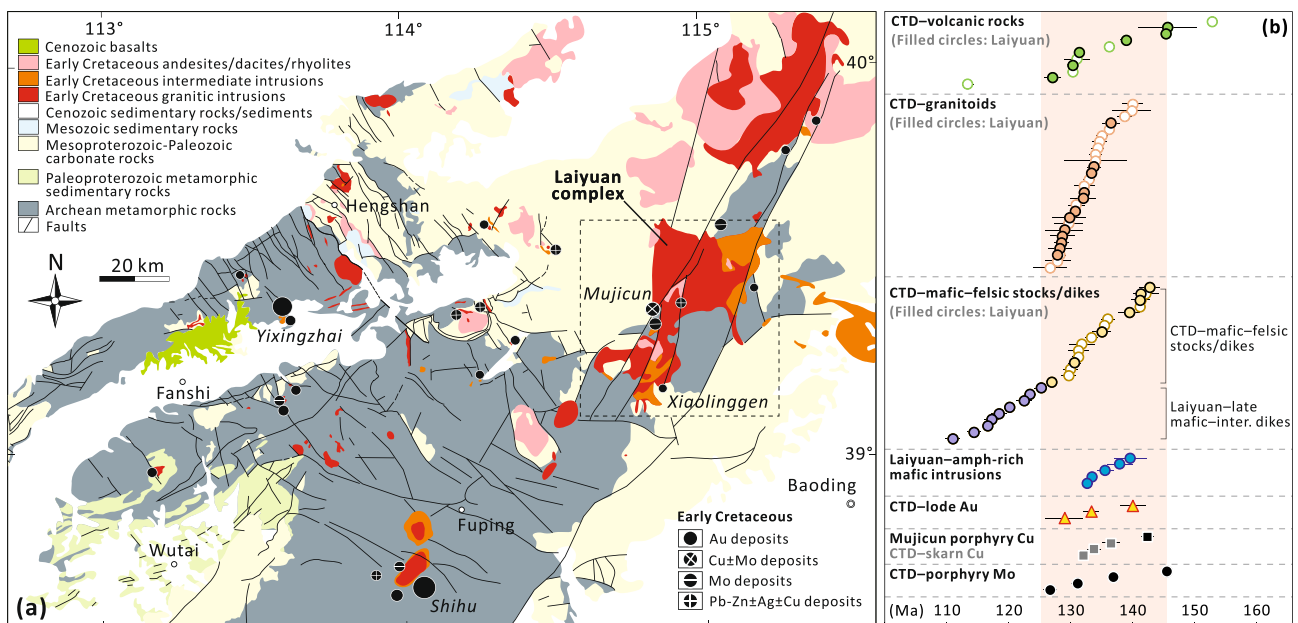


**Fig. 2** Geology and timing of the Early Cretaceous magmatism and mineralization in the central Taihangshan district (CTD). **a** Regional geological map (modified after Zhang et al. 2017). **b** Summary of

reliable isotopic ages of the Early Cretaceous magmatic rocks and related hydrothermal ore deposits (see Table S1 for data source of the isotopic ages)

et al. 2012; Zhang et al. 2017). The auriferous quartz-sulfide veins are spatially associated with broadly coeval mafic to felsic dikes (see Fig. S1 regarding the range of magma compositions). The largest Au deposit (Yixingzhai; ~ 94 t Au; ~ 140 Ma) is temporally bracketed by pre-ore and post-ore diorite dikes of similar isotopic ages. Auriferous quartz veins of the second largest Au deposit (Shihu; ~ 30 t Au; ~ 130 Ma) are spatially associated with numerous coeval quartz-diorite dikes, both being controlled by NNE- to NNW-trending faults (Wang et al. 2015). The auriferous quartz veins in the Xiaolinggen Au deposit and many pre-ore or syn-ore lamprophyre and diorite dikes consistently strike NW to NNW (Ding et al. 1992). The ~ 142 Ma Mujicun porphyry Cu–Mo deposit (Fig. 2a), containing ore reserves of ~ 20 Mt at 0.4 wt% Cu and 0.052 wt% Mo, is the only large Mesozoic porphyry Cu deposit in the NCC; this deposit is related to a diorite porphyry stock beneath an andesitic to dacitic volcanic edifice (Shi et al. 1980). There are also quite a few ~ 132–137 Ma skarn Cu–Fe deposits in the contact zone of early Cretaceous plutons and Mesoproterozoic–Paleozoic carbonate rocks (Shi et al. 1980). In addition, porphyry Mo-only deposits formed in the period of 127–145 Ma and are generally associated with porphyry intrusions with granodioritic to granitic compositions (Shi et al. 1980). In summary, lode Au deposits, porphyry/skarn Cu(–Mo) deposits and porphyry Mo-only deposits that extend throughout the CTD formed contemporaneously with the ~ 126–145 Ma magmatic rocks.

## Samples and methods

In this study, whole-rock geochemical data of variously evolved, early Cretaceous magmatic rocks in the CTD were compiled from the literature, including major and trace-element compositions of 218 samples and Sr–Nd isotopes of 113 samples (Tables S2 and S3). Twenty-five samples of amphibole-rich mafic–ultramafic intrusions and 16 samples of mafic to intermediate dikes in the Laiyuan complex were collected for petrographic study and laser-ablation inductively coupled-plasma mass-spectrometry (LA-ICP-MS) analysis of melt-, sulfide- and magnetite inclusions.

The LA-ICP-MS system used for inclusion analysis consists of a 193 nm ArF Excimer laser (GeolasPro system, Coherent, USA) coupled with a quadrupole mass spectrometer (Elan DRC-e, Perkin Elmer, Canada) hosted at the Bavarian Geoinstitute, University of Bayreuth. The sample chamber was flushed with He gas at a rate of 0.4 l/min, to which 5 ml/min H<sub>2</sub> gas was added on the way to the ICP-MS system. The ICP-MS system was tuned to a ThO rate of 0.10 ± 0.05% and a doubly charged Ca ions rate of 0.25 ± 0.05% based on measurements of the NIST SRM 610 standard. Isotopes analyzed include <sup>23</sup>Na, <sup>25</sup>Mg, <sup>27</sup>Al, <sup>30</sup>Si,

<sup>31</sup>P, <sup>32</sup>S, <sup>35</sup>Cl, <sup>39</sup>K, <sup>43</sup>Ca, <sup>49</sup>Ti, <sup>51</sup>V, <sup>53</sup>Cr, <sup>55</sup>Mn, <sup>57</sup>Fe, <sup>59</sup>Co, <sup>60</sup>Ni, <sup>65</sup>Cu, <sup>66</sup>Zn, <sup>75</sup>As, <sup>82</sup>Se, <sup>85</sup>Rb, <sup>88</sup>Sr, <sup>89</sup>Y, <sup>90</sup>Zr, <sup>93</sup>Nb, <sup>98</sup>Mo, <sup>105</sup>Pd, <sup>107</sup>Ag, <sup>110</sup>Cd, <sup>121</sup>Sb, <sup>125</sup>Te, <sup>133</sup>Cs, <sup>137</sup>Ba, <sup>140</sup>Ce, <sup>197</sup>Au, <sup>181</sup>Ta, <sup>205</sup>Tl, <sup>208</sup>Pb, <sup>209</sup>Bi, <sup>232</sup>Th and <sup>238</sup>U. Dwell time for different isotopes varied from 10 to 50 ms, except for <sup>197</sup>Au in a small subset of melt inclusions, for which 300 ms was taken and meanwhile only <sup>39</sup>K, <sup>65</sup>Cu and <sup>181</sup>Ta were analyzed. <sup>197</sup>Au signals were corrected for <sup>181</sup>Ta<sup>16</sup>O interference based on drift-corrected oxide production rates determined by analyzing a synthetic, Ta-rich (1300 µg/g Ta) silicate glass, which suggested an artificial Au signal of 7.6 × 10<sup>−4</sup> µg/g Au per µg/g Ta. The contribution of <sup>65</sup>Cu<sup>40</sup>Ar interference on the Pd concentrations measured in Cu-bearing sulfide inclusions was numerically subtracted with an equation similar to that given in Chang and Audétat (2018). Sulfur and Cl concentrations in melt inclusions were quantified using the approach of Rottier and Audétat (2019). The laser was operated at 5–10 Hz with an energy density of 3–10 J/cm<sup>2</sup>, creating laser pits of 10–120 µm in diameter. Unexposed melt inclusions were drilled out as a whole together with host mineral. The ablated host was then subtracted numerically from the LA-ICP-MS mixed signals until constraints for the internal standard were matched (Chang and Audétat 2021). The NIST610 glass was used as an external standard. Internal standardization of melt inclusions hosted in clinopyroxene and hornblende was based on the trend of SiO<sub>2</sub> vs. Al<sub>2</sub>O<sub>3</sub> displayed by whole-rock data, whereas the whole-rock trend of SiO<sub>2</sub> vs. CaO or a fixed content of 13 wt% Al<sub>2</sub>O<sub>3</sub> were used for apatite- and quartz-hosted melt inclusions, respectively. In all cases, the sum of major element oxides was normalized to 100 wt% anhydrous. Because olivine-hosted melt inclusions experienced post-entrapment modifications, only incompatible elements were quantified using a fixed value of an incompatible element as internal standard without normalizing the sum of major element oxides to 100 wt% (Chang and Audétat 2021). Uncertainties associated with the analyses of apatite- and quartz-hosted melt inclusions are estimated at 5–20 wt%, except for elements close to the limit of detection. For melt inclusions hosted in clinopyroxene and hornblende, the uncertainties tend to be higher (up to 30–50%) owing to the sensitivity of the host subtraction to minor variations in mineral composition (Chang and Audétat 2021). Uncertainties of the quantified incompatible element concentrations in olivine-hosted melt inclusions are estimated at ca. 20–25% (Chang and Audétat 2021). Sulfide inclusions were quantified using a synthetic pyrrhotite (Laflamme Po724 SRM of the Memorial University of Newfoundland) as an external standard for Fe, S and Pd, and NIST 610 for the other elements, and by normalizing the sum of S, Fe, Co, Ni and Cu to 100 wt%. Analyses of magnetite inclusions were quantified using the natural ilmenite sample KI-2193 and the NIST 610 glass as external standards. Uncertainties associated with the analyses of

sulfide inclusions and magnetite inclusions are ca. 5–10% (Zhang and Audétat 2017; Chang and Audétat 2018).

## Results

### Whole-rock geochemistry

This part mainly compares whole-rock geochemistry of the 126–145 Ma magmatic rocks throughout the CTD (Fig. 2). Whole-rock geochemistry of variously evolved magmatic rocks in the Laiyuan complex was summarized and discussed in Chang et al. (2021). Notably, 126–145 Ma magmatic rocks with <55 wt% SiO<sub>2</sub> and 110–125 Ma mafic to intermediate dikes have been reported only from the Laiyuan complex. The data compilation suggests that Cu/Au ore-related stocks/dikes and all the other 126–145 Ma intermediate to felsic rocks from different parts of the CTD show highly comparable whole-rock elemental and Sr–Nd isotopic compositions (Figs. 3 and S2). The intermediate to felsic rocks generally display more differentiated trace-element patterns than the mafic rocks (Fig. 3c, d). Strontium–Nd isotopic compositions of the intermediate to felsic rocks largely overlap with those of the mafic rocks, both showing low  $\epsilon_{\text{Nd}}(t)$  values (Fig. 3e). Many of the intermediate to felsic rocks, particularly the Cu/Au ore-related stock/dikes, have elevated Sr/Y ratios (Figs. 3f and S3a). In addition, the intermediate to felsic rocks show horizontal to decreasing Dy/Yb with increasing SiO<sub>2</sub> (Fig. S3b).

### Petrography of sulfide inclusions and silicate melt inclusions

The petrography and petrogenesis of mafic to intermediate rocks hosting silicate melt- and sulfide inclusion are briefly summarized here (see Chang et al. 2021 for more details), including amphibole-rich mafic–ultramafic rocks from the Longmengou and Yaogou units (~133–140 Ma), early mafic to intermediate dikes (~126–145 Ma) and late mafic dikes (~110–125 Ma). Various types of cumulitic and gabbroic rocks at Longmengou and Yaogou crystallized from olivine and clinopyroxene-bearing basaltic magma bodies emplaced in the upper crust. The ultramafic, cumulitic rocks (i.e., hornblendites and pyroxenites) formed via reaction replacement of early-crystallized olivine and clinopyroxene by amphibole-rich assemblages (amphibole, clinopyroxene, phlogopite and  $\pm$  plagioclase) in olivine and clinopyroxene-rich zones, whereas gabbroic rocks (i.e., porphyritic hornblende gabbros, equigranular hornblende gabbros, and acicular hornblende gabbros) formed in zones containing less olivine and clinopyroxene. The early and late mafic dikes crystallized phenocrysts of olivine, clinopyroxene  $\pm$  amphibole. The late mafic dikes also entrained

some cogenetic xenoliths of clinopyroxene cumulates and reaction-replacement hornblendites. The early intermediate dikes crystallized phenocrysts of amphibole and plagioclase.

Olivine and clinopyroxene in the cumulitic and gabbroic rocks at Longmengou and Yaogou (Fig. 4a) are generally devoid of sulfide inclusions; only one single, small (~15  $\mu\text{m}$ ) inclusion was found in an olivine crystal after careful examination of more than 40 thick sections. In contrast, the amphibole-rich assemblages in the cumulitic and some gabbroic rocks contain abundant sulfide inclusions (Fig. 4b, c); most unshielded magmatic sulfides in fresh cumulitic samples are also well preserved, but those in the gabbroic rocks are generally altered (Fig. S4). The volumetric abundances of magmatic sulfides in two very fresh cumulitic rocks have been determined at  $0.23 \pm 0.05$  vol% and  $0.18 \pm 0.01$  vol%, respectively (Chang et al. 2021). Coarsely crystallized melt inclusions are common in olivine crystals of the cumulitic rocks (Fig. 4d). In the early mafic and intermediate dikes (Fig. 4e), sparse sulfide inclusions occur in amphibole phenocrysts. In the late mafic dikes (Fig. 4f, g), sulfide inclusions are very abundant in some clinopyroxene phenocrysts (Fig. 4h), and they are also common in amphibole phenocrysts (Fig. 4i). Clinopyroxene, amphibole and apatite in xenoliths of the late mafic dikes (e.g., Fig. 4g) also commonly contain sulfide inclusions. Crystallized melt inclusions were observed in clinopyroxene, amphibole and apatite phenocrysts of the late mafic dikes (Fig. 4i, j) and in clinopyroxene and apatite of the xenoliths. Notably, in all the investigated samples exposed sulfide inclusions are dominated by pyrrhotite and contain minor amounts of chalcopyrite and pentlandite (e.g., Fig. 4b, c).

### Composition of mafic melt inclusions

The composition of melt inclusions in the studied mafic to intermediate rocks was partly reported in Chang et al. (2021). Copper, Au, S and Cl concentrations in these melt inclusions are newly obtained in this study by LA-ICP-MS analysis of entire, unexposed melt inclusions without prior re-homogenization (Tables 1 and S4). The study of Chang et al. (2021) showed that the trace-element patterns of olivine-hosted melt inclusions from the early amphibole-rich mafic–ultramafic intrusions and clinopyroxene-hosted melt inclusions from the late mafic dikes (plus the entrained xenoliths) match well with that of early and late mafic whole rocks, respectively. Copper concentrations in olivine-hosted melt inclusions at Yaogou and Longmengou and the clinopyroxene-hosted melt inclusions in late dikes are 150–230  $\mu\text{g/g}$  ( $n = 8$ ), 33–48  $\mu\text{g/g}$  ( $n = 7$ ) and <16–130  $\mu\text{g/g}$  ( $n = 48$ ), respectively. The large Cu variation in the clinopyroxene-hosted melt inclusions likely reflect the fact that sulfide saturation was already attained during the crystallization of clinopyroxene phenocrysts. A few particularly large melt

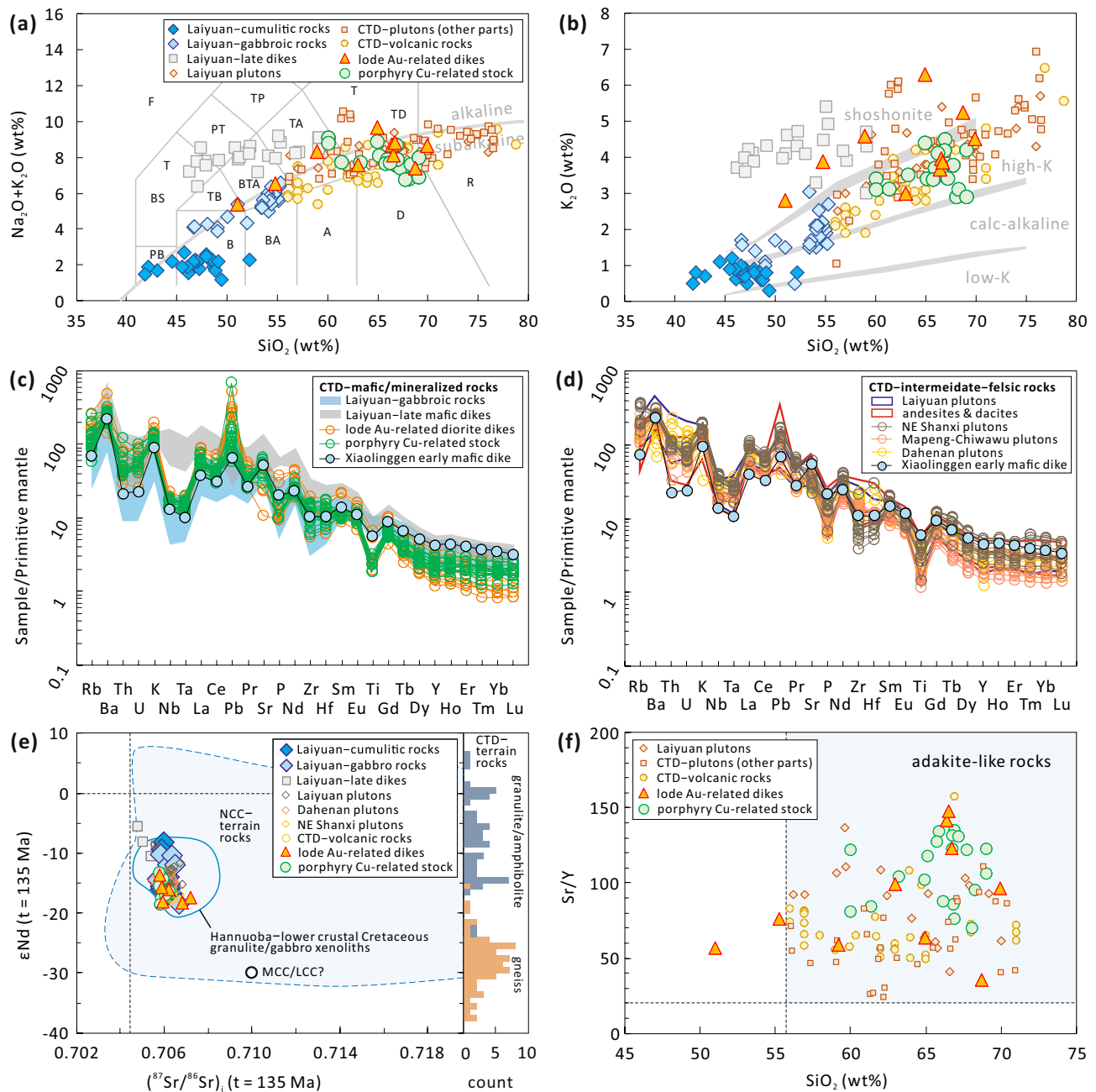


**Fig. 3** Whole-rock geochemistry of early Cretaceous magmatic rocks in the central Taihangshan district (CTD). These rocks formed mostly in the period of 126–145 Ma, except for some late mafic to intermediate dikes. **a, b** The magmatic rocks are alkali-rich, and belong mostly to high-K calc-alkaline or shoshonite series. **c, d** Various types of early magmatic rocks from different parts of the CTD show very similar primitive mantle-normalized trace-element patterns, whereas the late mafic dikes have distinctive trace-element patterns. **e** The early magmatic rocks show similar Sr–Nd isotopic compositions, but the late mafic dikes trend towards lower  $(^{87}\text{Sr}/^{86}\text{Sr})_i$  and higher  $\epsilon\text{Nd}$ . Sr–

Nd isotopic compositions of the Hannuoba lower crustal Cretaceous mafic xenoliths, Archean to Paleoproterozoic metamorphic terrain rocks in the CTD and throughout the North China Craton (NCC) are shown for comparison (Liu et al. 2010). Note the extremely heterogeneous Sr–Nd isotopic compositions of the terrain rocks. **f** The early intermediate to felsic magmatic rocks are characterized by adakite-like, high Sr/Y ratios (Richards and Kerrich 2007). In panels **c, d** and **f** highly differentiated rocks (> 72 wt% SiO<sub>2</sub>) that experienced strong plagioclase fractionation were not included for simplicity

inclusions were selected for Au analysis to reach as low detection limits as possible, including five olivine-hosted melt inclusions (~45–80 μm in diameter) from Yaogou, and

six clinopyroxene-hosted melt inclusions (~60–72 μm) from late dikes. Only the largest of the five olivine-hosted melt inclusions from Yaogou returned a measurable Au signal

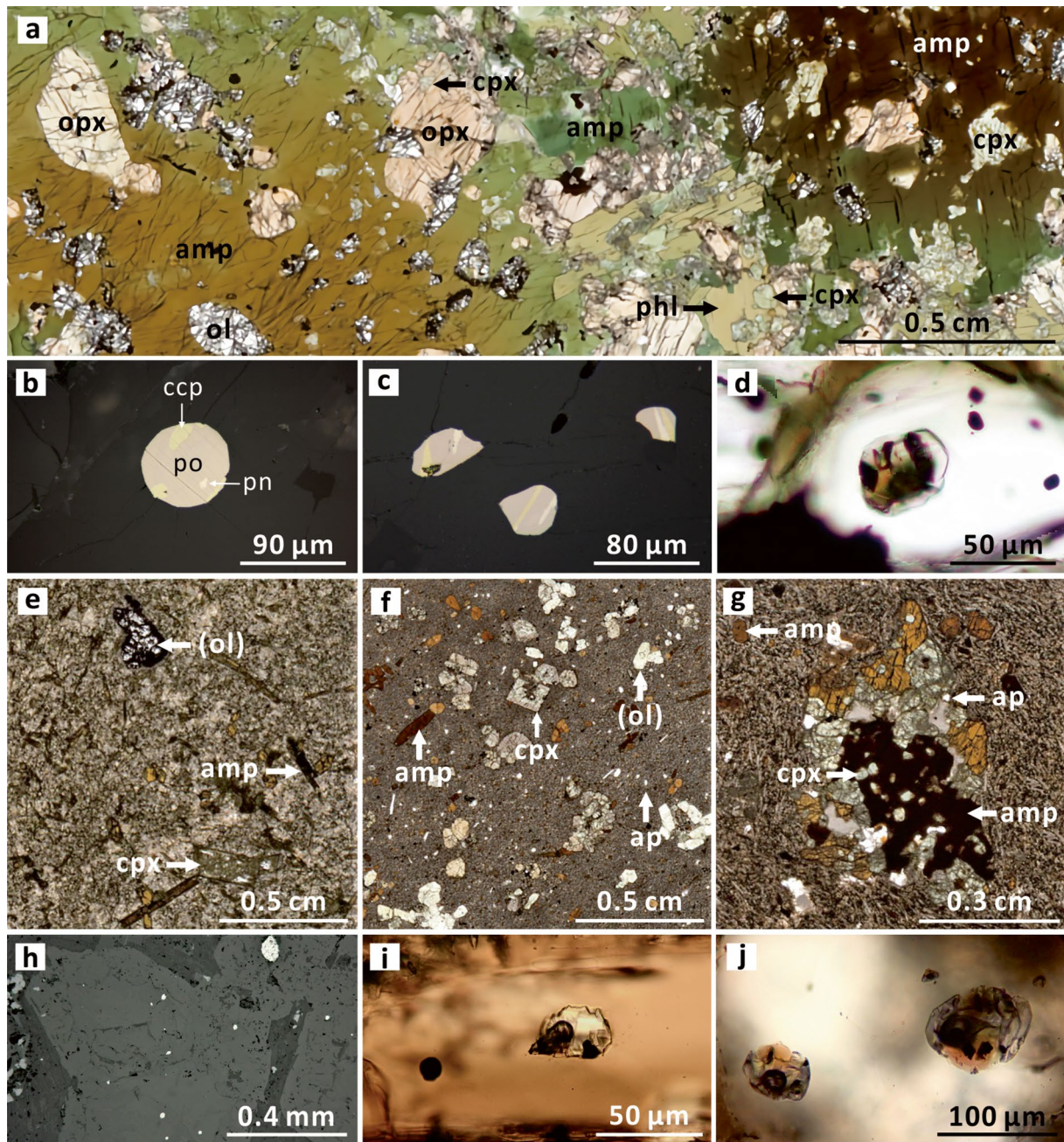


**Fig. 4** Petrography of mafic-ultramafic rocks of the Laiyuan complex. **a** A typical hornblende from Longmengou, showing reaction replacement of early-crystallized olivine and clinopyroxene by orthopyroxene, phlogopite and amphibole. **b, c** Magmatic sulfide inclusions in amphibole of a hornblende from Yaogou. Note the reproducibility of sulfide phase proportions. **d** A fully crystallized melt inclusion hosted in olivine of a hornblende from Yaogou. The small, opaque inclusions on the right are Cr-rich magnetite. **e** An early mafic dike from Xiaolinggen, characterized by phenocrysts of olivine, clinopyroxene and  $\pm$  amphibole set in a fine-grained matrix.

**f** A late mafic dike containing phenocrysts of clinopyroxene, olivine, hornblende and apatite. **g** A reaction-replacement hornblende xenolith in a late mafic dike. **h** Numerous, exposed sulfide inclusions in clinopyroxene phenocrysts of a late mafic dike. **i** A crystallized melt inclusion (on the right) and an unexposed sulfide inclusion (on the left) hosted in a hornblende phenocryst of a late mafic dike. **j** Two large, crystallized melt inclusions hosted in a clinopyroxene phenocryst of a late mafic dike. *ap* apatite; *cpx* clinopyroxene; *ccp* chalcocopyrite; *amp* amphibole; *ol* altered olivine; *opx* orthopyroxene; *phl* phlogopite; *pn* pentlandite; *po* pyrrhotite

(5 ng/g Au), whereas the other melt inclusions gave detection limits of 10–20 ng/g. Gold concentrations in the six clinopyroxene-hosted melt inclusions from late dikes were

all below detection limits of 7–32 ng/g. Nine olivine-hosted melt inclusions from Yaogou, two olivine-hosted melt inclusions from Longmengou, and 12 clinopyroxene-hosted

**Table 1** Alkalis, S, Cl, Cu and Au concentrations in mafic melt inclusions at Laiyuan

Sample type	SiO <sub>2</sub> <sup>a</sup>	K <sub>2</sub> O	Na <sub>2</sub> O <sup>b</sup>	S	Cl	Cu	Au
Yaogou ol-hosted MI's	46–53	3.1–4.5	1.9–4.7	0.15–0.23	0.10–0.18	150–230	~5
Longmengou ol-hosted MI's	46–53	2.0–2.4	2.7–3.7	0.14–0.24	0.11	33–48	n.a
Late-dike cpx-hosted MI's	46–53	3.0–5.9	3.1–6.5	0.12–0.24	0.15–0.20	<16–130	<7

SiO<sub>2</sub>, K<sub>2</sub>O, Na<sub>2</sub>O, S and Cl in wt%, Cu in µg/g, and Au in ng/g

ol olivine; cpx clinopyroxene; MI's melt inclusions; n.a. not analyzed

<sup>a</sup>The range of SiO<sub>2</sub> contents were roughly constrained by corresponding whole-rock data

<sup>b</sup>Na<sub>2</sub>O contents of some ol-hosted MI's may be too low due to Na loss (Chang et al. 2021)

melt inclusions from late dikes were analyzed for S and Cl. Obtained sulfur concentrations are 0.15–0.23 wt% ( $n=9$ ), 0.14–0.24 wt% ( $n=2$ ) and 0.12–0.24 wt% ( $n=12$ ), respectively. Based on the volumetric abundance of well-preserved magmatic sulfides in two Longmengou and Yaogou cumulitic rocks (see above), the petrogenesis of these cumulitic rocks and the sulfur content of the sulfides, a similar sulfur content of the mafic melts is estimated (0.15–0.29 wt% S). Chlorine concentrations in the melt inclusions are 0.1–0.2 wt%, but uncertainties of these measurements may be large because the Cl signals are close to the limit of detection.

### Composition of magmatic sulfide inclusions

A total of 115 entire, unexposed sulfide inclusions were analyzed (Fig. 5; Table S5). The bulk composition of these sulfide inclusions generally falls in or close to the field of monosulfide solid solution (MSS) on the ternary phase diagram at the temperature of 1000 °C (Fig. 5a, b). Copper concentrations in sulfide inclusions from Longmengou are lower than those from Yaogou (Fig. 5c). This result is consistent with the lower Cu content of olivine-hosted melt inclusions from Longmengou (Table 1). Apart from this, sulfide inclusions from different rock types at Longmengou or Yaogou are compositionally similar (Fig. 5d–h). Copper concentrations in sulfide inclusions from the early mafic to intermediate dikes decrease from 7.8 to 0.5 wt% with decreasing Ni concentration (Fig. 5c), whereas Cu concentrations in sulfide inclusions from the late mafic dikes (plus cogenetic xenoliths) decrease less strongly from 4.2 to 0.5 wt%. Palladium concentrations in sulfide inclusions from the late mafic dikes also decrease with decreasing Ni concentration (Fig. 5d). By contrast, Au, Ag, Bi and Te concentrations in sulfide inclusions do not vary systematically with Ni concentration (Fig. 5e–h).

### Thermobarometry

Crystallization P–T conditions of the amphibole-rich mafic–ultramafic intrusions at Longmengou and Yaogou and the late mafic dikes were constrained by Chang et al. (2021). The early-crystallized olivine and clinopyroxene

in the amphibole-rich mafic–ultramafic rocks likely crystallized at  $\geq 1030$ –1075 °C and 0.3–0.6 GPa, whereas amphibole-rich assemblages and some near-solidus minerals (e.g., quartz and titanite) in these rocks crystallized after final emplacement of the mafic magmas at 690–1040 °C and 0.1–0.2 GPa. Clinopyroxene phenocrysts in the late mafic dikes and xenoliths in these dikes likely crystallized at 990–1140 °C and 0.4–1.3 GPa.

The oxidation state of magmas was constrained by the FeTiMM magnetite-liquid oxybarometer (Arató and Audétat 2017). The magnetite composition was obtained from LA-ICP-MS analyses of entire, unexposed magnetite inclusions to circumvent re-equilibration and exsolution effects during cooling (Table S6), and the composition of the liquid was constrained from melt inclusion and whole-rock data. Detailed calculation procedures and results are presented in Table S7. The uncertainty of the FeTiMM oxybarometer is  $\pm 0.5$  log units, but due to the relatively large uncertainty associated with the quantification of the liquid the overall uncertainty of the present application may reach  $\pm 1.0$  log units. The oxygen fugacity of magmas that crystallized olivine crystals in a Yaogou hornblende was constrained at  $\Delta\text{FMQ} + 2.6$  (i.e., 2.6 log units above the fayalite–magnetite–quartz buffer). In addition, the titanite + quartz  $\pm$  magnetite assemblages with clinopyroxene in the matrix of porphyritic hornblende gabbros from Longmengou also suggest a relatively high oxidation state (Wones 1989). Compositions of melt inclusions and magnetite inclusions hosted in quartz phenocrysts (or xenocrysts) in two early intermediate to felsic dikes from Xiaolinggen also returned a relatively high oxygen fugacity of  $\Delta\text{FMQ} + 2.3$ –2.6. By contrast, a lower oxygen fugacity of  $\Delta\text{FMQ} + 1.1$ –1.7 was obtained from the compositions of melt inclusions and magnetite inclusions in clinopyroxene phenocrysts of the late mafic dikes.

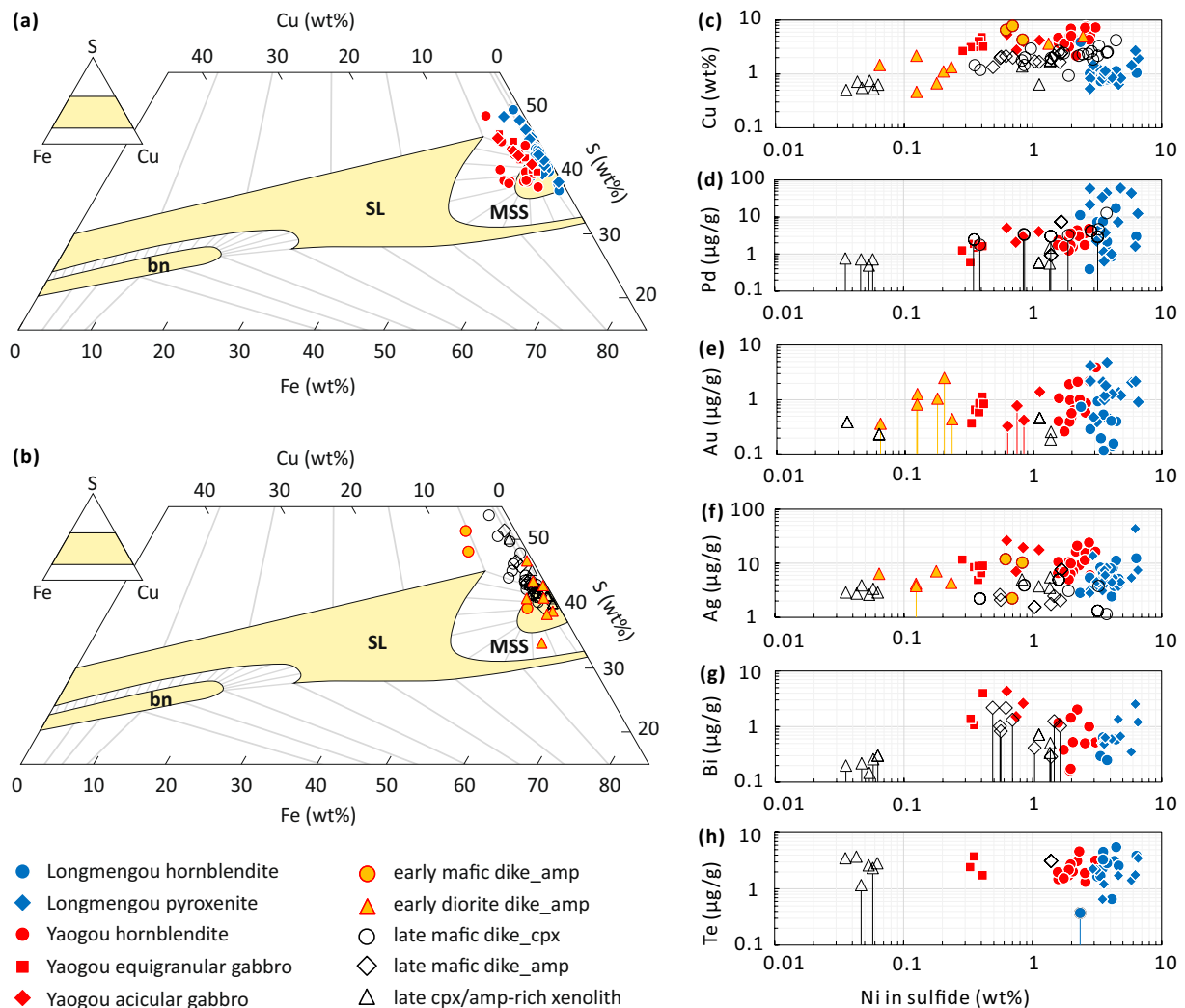


**Fig. 5** Composition of sulfide inclusions. **a, b** Bulk compositions of sulfide inclusions, plotted on the Cu–Fe–S diagram at 1 bar and 1000 °C (Kullerud et al. 1969). The displacement of some data points outside the MSS field towards higher S contents is due to the relatively large uncertainty associated with S analyses by LA-ICP-MS.

**c–h** Copper, Pd, Au, Ag, Bi and Te concentrations as a function of Ni concentration. Data points connected with a downward, vertical line signify detection limits. *bn* bornite solid solution; *MSS* monosulfide solid solution; *SL* sulfide liquid

## Discussion

### Petrogenesis and fertility of early Cretaceous magmatic rocks in the CTD

Our compiled whole-rock geochemical data suggest that the majority of 126–145 Ma intermediate to felsic rocks throughout the CTD display very similar elemental and Sr–Nd isotope compositions to the Laiyuan equivalents (Figs. 3 and S2). This geochemical uniformity is better explained by the differentiation model of SCLM-derived mafic magmas than by the anatexis model of ancient lower crust (Chang et al. 2021), as partial melting of the heterogeneous metamorphic basement of the CTD (Tang and Santosh

2018) would be expected to produce melts with rather different elemental and isotopic signature at different localities. Therefore, the 126–145 Ma magmatic rocks throughout the CTD likely formed during the transition from a compressional to an extensional regime (Chang et al. 2021), presumably induced by the retreat of the low-angle subducting Paleo-Pacific slab, whereas the 110–125 Ma mafic to intermediate dikes might result from local mantle perturbations due to continuous slab retreat.

The elevated Sr/Y ratios of many intermediate rocks in the CTD (Figs. 3f and S3a), particularly of the Cu/Au ore-related stock/dikes, suggest that the parental mafic magmas of these rocks probably experienced major amphibole ( $\pm$  garnet) fractionation and only limited plagioclase

fractionation (Richards and Kerrich 2007). The constant to slightly decreasing Dy/Yb ratios as a function of increasing SiO<sub>2</sub> preclude major garnet fractionation (Fig. S3b).

Porphyry/skarn Cu, porphyry Mo-only and lode Au deposits that occur throughout the CTD formed during the same time interval as the ~126–145 Ma magmatic rocks (Fig. 2). The porphyry Cu/Mo deposits are clearly related to specific porphyry magmas. By contrast, it is not straightforward to conclude that ore-forming fluids of the lode Au deposits were derived from the ~126–145 Ma magmatic rocks, as the genetic relationship between lode Au mineralization and specific magmas is difficult to be established based on geological relationships. However, the lode Au deposits in the CTD, including the two largest Yixingzhai and Shihu Au deposits, are mostly hosted in the Neo-Archean to Paleoproterozoic amphibolite- to granulite-facies metamorphic rocks, which renders the metamorphic-related orogenic model (Groves et al. 1998) impossible to explain their genesis. Moreover, available geochemical evidence suggests that the lode Au deposits were derived dominantly from magmatic fluids (Cao et al. 2012; Zhang et al. 2017). It is thus argued that the ~126–145 Ma magmas were responsible for the lode Au mineralization.

### Behavior of metals during the evolution of magmas in the CTD

The timing of sulfide saturation and the type of saturated sulfides strongly affect the metal budget of magmas (Li and Audétat 2012, 2015; Liu and Brenan 2015). Our petrographic observations suggest that the parental mafic magmas of the amphibole-rich mafic–ultramafic intrusions at Longmengou and Yaogou were undersaturated in sulfides during the crystallization of olivine and clinopyroxene, and then became sulfide-saturated during the crystallization of amphibole-rich assemblages. The magmas that formed the early mafic to intermediate dikes also reached sulfide saturation during or before the crystallization of amphibole phenocrysts. By contrast, the magmas of the late mafic dikes and cogenetic xenoliths already reached sulfide saturation during the crystallization of clinopyroxene. These results are consistent with the higher oxidation state (but similar sulfur content) of the early magmas (~ $\Delta\text{FMQ} + 2.5$ ) compared to the late magmas (~ $\Delta\text{FMQ} + 1.5$ ). Though the early mafic magmas had rather high oxidation state, the good match of measured sulfur content of olivine-hosted melt inclusions from Longmengou and Yaogou and calculated sulfur content of the mafic melts based on sulfide abundances in two cumulitic rocks suggest that the sulfur in the mafic magmas precipitated mostly in the form of sulfides.

The phase proportions within exposed sulfide inclusions (Fig. 4b, c) and the major element composition of entire, unexposed sulfide inclusions (Fig. 5a, b) suggest that the

sulfide inclusions consist dominantly of FeS with only small amounts of Cu and Ni. Because the host minerals crystallized at lower temperatures than the melting point of pyrrhotite ( $\geq 1190$  °C), all sulfide inclusions should have been trapped in the form of crystalline monosulfide solid solution (MSS). The Cu content of sulfide inclusions in the early mafic to intermediate dikes and the late mafic dikes (plus cogenetic xenoliths) decreases with decreasing Ni content (Fig. 5c), whereas the concentrations of Au, Ag, Bi and Te remain relatively stable (Fig. 5e–h). These trends agree with MSS being the dominant fractionating sulfide phase, as Au, Ag, Bi and Te partition more strongly into sulfide liquid and intermediate solid solution than is the case for Cu (Liu and Brenan 2015; Chang and Audétat 2018). Hence, if the sulfides would have precipitated in the form of sulfide liquid or intermediate solid solution, then the Au, Ag, Bi and Te contents of the sulfide inclusions would need to decrease even more rapidly than the Cu content.

A quantitative model similar to those described in Chang and Audétat (2018), Li et al. (2019) and Du and Audétat (2020) was developed to constrain the metal contents of residual melt during the evolution of the two magmatic episodes in the Laiyuan complex. The following parameters were chosen to best fit the data obtained from the two groups of mafic to intermediate rocks: (i) the relationship between magma crystallinity and SiO<sub>2</sub> content of silicate melt, (ii) the timing of sulfide saturation, (iii) the type of crystallized sulfide, (iv) the amount of crystallized sulfide, (v) partition coefficients of metals between sulfide and silicate melt, and (vi) the proportion of fractional versus equilibrium crystallized sulfide.

(i) The relationship between magma crystallinity, melt SiO<sub>2</sub> content and temperature was established on experimental data that reproduce the mineral crystallization sequence of olivine and clinopyroxene followed by amphibole (Holloway and Burnham 1972; Foden and Green 1992; Melekhova et al. 2015; Ulmer et al. 2018). The starting temperature was set to 1100 °C. Two separate fitting equations were obtained for fractional crystallization and equilibrium crystallization, respectively (Fig. S5). Both relationships were tested in the modeling (Figs. 6 and S6).

(ii) The early magmas reached sulfide saturation at 53 wt% melt SiO<sub>2</sub>, approximately at the onset of amphibole crystallization, whereas the late magmas were sulfide-saturated already from the beginning.

(iii) All of the crystallized sulfides were monosulfide solid solution (MSS).

(iv) Given that excess sulfur in the silicate melt was removed only in the form sulfides, the amount of crystallized sulfide depends on the melt sulfur content at the moment of sulfide saturation and the decrease of sulfur solubility during magma evolution. The starting sulfur content of both the early and late magmas was set to 0.2 wt%. The

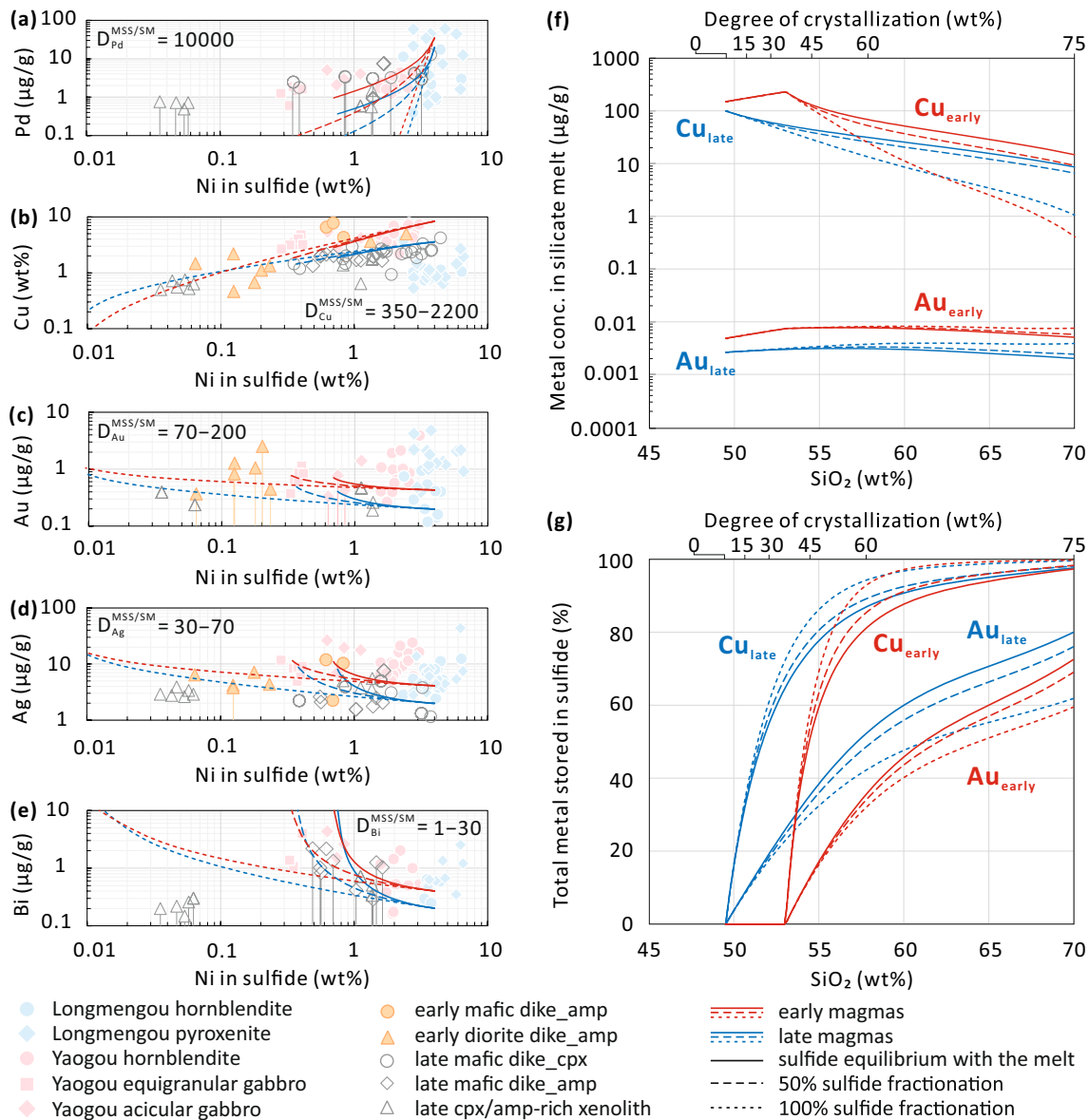


**Fig. 6** Quantitative model for the behavior of metals in the Laiyuan early and late magmas. **a–e** Measured versus modeled contents of Pd, Cu, Au, Ag, and Bi in MSS as a function of Ni content. The panels are ordered by decreasing sulfide-melt partition coefficient of the metals. Model calculations are shown for 0%, 50% and 100% equilib-

rium versus fractional sulfide crystallization. **f, g** Modeled metal content of residual melt, and percentages of metal stored in sulfides, as a function of magma crystallinity and melt SiO<sub>2</sub> content. The early and late magmas reached sulfide saturation at 49 wt% and 53 wt% SiO<sub>2</sub>, respectively

decrease of sulfur solubility during magma evolution was calculated using the models of Fortin et al. (2015) and Jugo et al. (2010), plus whole-rock trends of the corresponding magmatic rocks to link melt SiO<sub>2</sub> content to other major elements (similar to the approach elaborated in Chang and Audétat 2018).

(v) Partition coefficients of Cu, Au, Ag and Bi between MSS and silicate melts were calculated by equations given in Li and Audétat (2015). These calculations require independently constrained temperature, melt FeO<sub>tot</sub> content and oxygen fugacity. The temperature and melt FeO<sub>tot</sub> content

were linked to melt SiO<sub>2</sub> based on data from the above mentioned experiments and whole-rock trends of the corresponding magmatic rocks. The oxygen fugacity was fixed at  $\Delta FMQ + 2.5$  and  $\Delta FMQ + 1.5$  for the early and the late magmas, respectively. The partition coefficient of Pd between MSS and silicate melts was fixed at 10,000 based on available experimental data (Liu and Brenan 2015; Mungall and Brenan 2014; Li et al. 1996). The partition coefficients of the ore-forming metals between other minerals and silicate melts were set to zero. Since Ni also partitions strongly into silicate minerals (e.g., olivine, pyroxene and amphibole),

the partition coefficient and the starting melt content of Ni were adjusted to match the modeled range of other metals in sulfide within the range of 0.01–4 wt% Ni (see Figs. 6 and S6).

(vi) The proportion of fractional versus equilibrium crystallized sulfide was set to 0%, 50% or 100%.

The model reproduces well the evolution of Pd, Cu, Au, Ag and Bi contents of sulfide inclusions as a function of Ni content (Fig. 6a–e) and the Cu and Au contents of mafic silicate melt inclusions (Table 1). Therefore, the results justify the parameters used for the modeling. The models predict that the Cu content of the residual melt decreases by one to two orders of magnitude after reaching sulfide saturation, whereas the Au content of residual melt varies by no more than a factor of two (Fig. 6f). Accordingly, the precipitated sulfides have high Cu/Au ratios, and thus even fractional re-melting of such residual sulfides is unlikely to produce magmas with unusually high Au/Cu ratios.

### Formation of lode Au deposits: unusually Au-rich or voluminous magmas?

The compositions of silicate melt inclusions and sulfide inclusions suggest that the early mafic magmas contained only about 5 ng/g Au, which is similar to the global average of arc basalts (< 1–12 ng/g Au; GEOROC database) and mid-ocean-ridge basalts (< 1–5 ng/g Au; Jenner and O'Neill 2012). This result supports the argument that unusual Au enrichment in the SCLM source or in the derived primitive basaltic melts was not a prerequisite for the early Cretaceous lode Au mineralization in the NCC (Wang et al. 2020a). The modeling results presented above further suggest that differentiation of the early mafic magmas would neither cause significant Au enrichment nor significant Au depletion in the residual silicate melts (Fig. 6f). Taken together, the early mafic to intermediate magmas responsible for lode Au deposits in the CTD are unlikely to have been unusually enriched in Au before the exsolution of ore fluids. Consequently, large volumes of ore-forming magmas were required to form the lode Au deposits.

It is difficult to assign a particular magma composition as the source of the ore-forming fluids because the voluminous magmas seem to have been emplaced in the deep crust. Fluid inclusion studies suggest that the lode Au deposits from the CTD formed by means of liquid CO<sub>2</sub> phase-bearing, low-salinity fluids (e.g., Cao et al. 2012). The same is true for most other early Cretaceous lode Au deposits in other parts of the NCC (Zhu et al. 2015 and references therein). Therefore, ore-forming fluids of the lode Au deposits probably exsolved from magmas as a CO<sub>2</sub>-rich aqueous fluid phase. By contrast, CO<sub>2</sub>-rich fluid inclusions are rare in the early Cretaceous porphyry Cu–Mo or Mo-only deposits from CTD (e.g., Qu 2012) and in porphyry Cu deposits worldwide

(Kouzmanov and Pokrovski 2012). The source magmas that generated the ore fluids of the lode Au deposits thus may have been emplaced at much deeper levels than the typical paleodepths of 5–15 km for porphyry deposits (Sillitoe 2010; Fig. 7a), because the CO<sub>2</sub> content of deeply exsolved magmatic fluids tends to be higher than that of shallowly-exsolved magmatic fluids (Lowenstern 2001).

In addition, the early mafic magmas were hydrous (Chang et al. 2021) and contained high contents of S, Cl and alkalis (Table 1), comparable with porphyry Cu-related mafic magmas (Zhang and Audétat 2017) and some mafic arc magmas (Wallace 2005). These magmatic ingredients are equally important to generate lode Au-related ore fluids. Sulfur and Cl can enhance the efficiency of metal partitioning into aqueous fluids, and are also important agents for the transport of Au in aqueous fluids (Candela and Piccoli 2005). Zajacz et al. (2010) demonstrated experimentally that alkalis in magmas could also promote Au partitioning into exsolved fluids by increasing Au solubility in S-bearing aqueous fluids. In addition, lode Au deposits are first and foremost sulfur anomalies, considering that pyrite constitutes 3–20 vol% of the lode Au ores (Li et al. 2012). However, the late mafic magmas were also hydrous and contained relatively high abundances of S, Cl and alkalis (Table 1), but no lode Au deposits formed in this time interval. This may be due to a much smaller volume of these late magmas, though it is unclear how voluminous these late magmas were in the deep crust.

### Comparison with the giant Jiaodong Au province

A recent study suggests that SCLM-derived mafic dikes from the Jiaojia Au deposit with high Mg# close to primitive mantle melts contain only 1–3 ng/g Au (Wang et al. 2020b). Moreover, LA-ICP-MS analysis of unexposed sulfide inclusions in hornblende phenocrysts of intermediate dikes from the Guocheng Au deposit returned relatively low Au contents of 0.1–1.7 µg/g (Tan et al. 2012), which values are similar as those observed in this study (Fig. 5e). These results suggest that also the lode Au-related magmas in the Jiaodong district were not unusually Au-rich. We, therefore, propose that the much higher total Au reserve of the Jiaodong district (~ 4000 t Au) compared to the CTD (~ 150 t Au) is due to a much larger volume of SCLM-derived mafic to intermediate magmas. This inference is arguably supported by the higher abundance of lode Au-related mafic to intermediate dikes in many large lode gold deposits of the Jiaodong district, and is consistent with the stronger lithosphere modification underneath the Jiaodong district (Fig. 7b, c; Zhu et al. 2011). The ancient SCLM beneath the Jiaodong district completely vanished and even the crust was partly removed during the formation of the Jiaodong lode Au deposits (Zhu et al. 2011), thus more melts should have

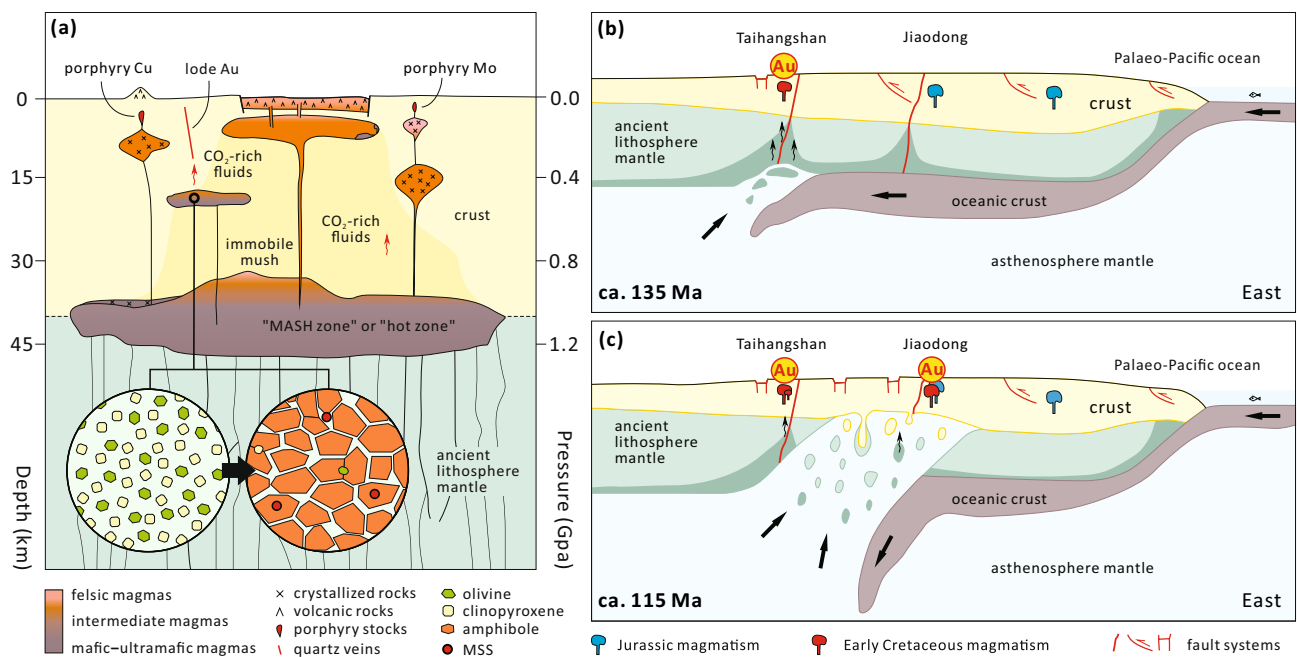


**Fig. 7** Tectono-magmatic model for lode Au mineralization in the North China Craton. **a** Early Cretaceous magma evolution and magmatic-hydrothermal ore formation in the central Taihangshan district. Mantle-derived basaltic magmas emplaced in the middle to lower crust experienced significant fractionation of olivine and clinopyroxene, followed by amphibole-dominated mineral assemblages to produce evolved magmas with adakite-like signatures. Abundant magmatic sulfides precipitated together with the amphibole. Intermediate to felsic magma bodies emplaced in the upper crust led to the for-

mation of porphyry Cu/Mo deposits, whereas mafic to intermediate magmas accumulated in the middle to lower crust favored the exsolution of CO<sub>2</sub>-rich aqueous fluids responsible for the formation of lode Au deposits. **b, c** Schematic tectonic reconstructions of early Cretaceous magmatism and lode Au mineralization in the North China Craton. The gradual younging trends of the early Cretaceous magmatism and lode Au mineralization from the central Taihangshan district to the Jiaodong district are in agreement with eastward slab rollback

been generated and should have accumulated at deep crustal levels beneath the Jiaodong district.

### Why no early Cretaceous giant porphyry Cu deposits in the NCC?

In addition to the numerous lode Au deposits, abundant Fe skarn, porphyry Mo-only and hydrothermal Ag–Pb–Zn deposits formed during the early Cretaceous craton destruction of the NCC (Fig. 8; Zhu et al. 2019). However, only one medium-sized porphyry Cu deposit and abundant small Cu–Fe skarn deposits have been recognized in the NCC (Shi et al. 1980; Chang et al. 2020; Yang and Cooke 2020). Our preliminary results suggest that SCLM-derived mafic magmas related to the lode Au deposits are hydrous, oxidized and relatively rich in S and Cl, which properties should also favor the formation of porphyry Cu deposits (Audétat and Simon 2012). The formation of giant, early Cretaceous porphyry Cu deposits in the NCC could have been suppressed by the intense extensional setting during the craton destruction. Porphyry Cu deposits are related to upper crustal, intermediate magma chambers situated at 5–15 km depth (Sillitoe 2010), but very strong extensional settings promote the

formation of very shallow crustal magma chambers that tend to erupt explosively, in which case the Cu-bearing magmatic fluids are lost to the atmosphere (cf. Sillitoe 2018). In addition, the occurrence of abundant early Cretaceous volcanic rocks and porphyry Mo-only deposits suggests that the lack of giant porphyry Cu deposits cannot be fully explained by regional uplift and erosion.

### Conclusions

The mafic to intermediate magmas genetically related to lode Au deposits were derived from partial melts of metasomatized subcontinental lithosphere mantle, and generally experienced deep olivine and clinopyroxene fractionation followed by amphibole-dominated fractionation. The magmas did not become enriched in Au due to relatively early saturation of MSS. Accumulation of large volumes of magmas in the middle to lower crust through trans-lithospheric faults was likely the key to Au mineralization. The lode Au-related magmas were hydrous, oxidized and relatively rich in S and Cl, which properties promoted the production of auriferous ore fluids. The strong extensional tectonic setting

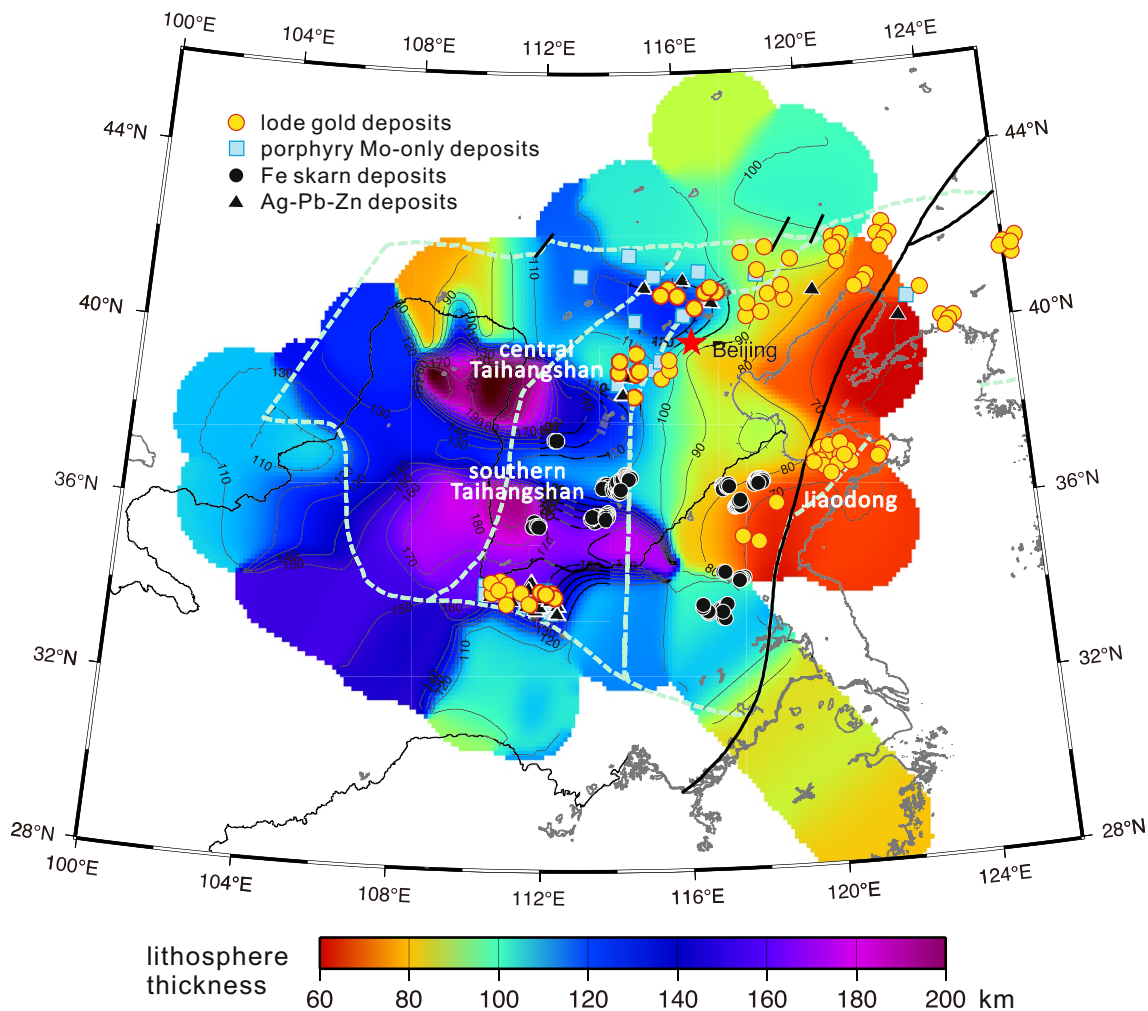


**Fig. 8** Lithosphere thickness and spatial distribution of late Mesozoic hydrothermal ore deposits in the North China Craton. Modified after Zheng et al. (2016)

associated with craton thinning and destruction that favored the formation of lode Au deposits was likely detrimental for the formation of giant porphyry Cu deposits.

**Supplementary Information** The online version contains supplementary material available at <https://doi.org/10.1007/s00410-021-01824-2>.

**Acknowledgements** Our thanks go to Si-Yuan Li, Wen-Sheng Gao, Dong-Yang Zhang, Guo-Xi Ma and Jian-Ye Ren for their help in organizing and conducting the field work, to Zhuang Duan, Ju-Quan Zhang and Zhan-Ke Li for providing electronic versions of geological maps, and to Hong-Rui Fan for fruitful discussions. Larry Meinert is appreciated for comments on an early version of the manuscript. Jean Cline and an anonymous reviewer are acknowledged for their helpful reviewer comments.

**Funding** Open Access funding enabled and organized by Projekt DEAL. Research work was financially supported by the Ministry of Science and Technology of China (2016YFC0600104), the 111 Project and the GPMR State Key Laboratory (MSFGPMR03). Jia Chang was funded by the China Scholarship Council, the Newmont Mining

Corporation Fund (SEG 2018 Student Research Grant program), the China Postdoctoral Science Foundation Grant (2019M662739) and the Postdoctoral Innovative Talents Support Program (BX20200311).

**Open Access** This article is licensed under a Creative Commons Attribution 4.0 International License, which permits use, sharing, adaptation, distribution and reproduction in any medium or format, as long as you give appropriate credit to the original author(s) and the source, provide a link to the Creative Commons licence, and indicate if changes were made. The images or other third party material in this article are included in the article's Creative Commons licence, unless indicated otherwise in a credit line to the material. If material is not included in the article's Creative Commons licence and your intended use is not permitted by statutory regulation or exceeds the permitted use, you will need to obtain permission directly from the copyright holder. To view a copy of this licence, visit <http://creativecommons.org/licenses/by/4.0/>.

## References

- Arató R, Audétat A (2017) FeTiMM—a new oxybarometer for mafic to felsic magmas. *Geochem Perspect Lett* 5:19–23. <https://doi.org/10.7185/geochemlet.1740>
- Audétat A, Simon AC (2012) Magmatic controls on porphyry copper genesis. *SEG Spec Publ* 16:553–572. <https://doi.org/10.5382/SP.16.21>
- Candela PA, Piccoli PM (2005) Magmatic processes in the development of porphyry-type ore systems. *Econ Geol* 100:25–38. <https://doi.org/10.5382/AV100.03>
- Cao Y, Carranza EJM, Li S, Yao M, Zhang H (2012) Source and evolution of fluids in the Shihu gold deposit, Taihang Mountains, China: evidence from microthermometry, chemical composition and noble gas isotope of fluid inclusions. *Geochem Explor Environ Anal* 12(2):177–191. <https://doi.org/10.1144/1467-7873/11-MINDEP-073>
- Chang J, Audétat A (2018) Petrogenesis and metal content of hornblende-rich xenoliths from two Laramide-age magma systems in southwestern USA: insights into the metal budget of arc magmas. *J Petrol* 59(10):1869–1898. <https://doi.org/10.1093/ptrology/egy083>
- Chang J, Audétat A (2021) LA-ICP-MS analysis of crystallized melt inclusions in olivine, plagioclase, apatite and pyroxene: Quantification strategies and effects of post-entrapment modifications. *J Petrol* 62(4):egaa085. <https://doi.org/10.1093/ptrology/egaa085>
- Chang Z, Shu Q, Meinert LD (2020) Skarn deposits of China. *SEG Spec Publ* 22(22):189–234. <https://doi.org/10.5382/SP.22.06>
- Chang J, Audétat A, Li JW (2021) In-situ reaction-replacement origin of hornblendites in the Early Cretaceous Laiyuan complex, North China Craton, and implications for its tectono-magmatic evolution. *J Petrol* 62(5):egab030. <https://doi.org/10.1093/ptrology/egab030>
- Chiaradia M (2014) Copper enrichment in arc magmas controlled by overriding plate thickness. *Nat Geosci* 7(1):43–46. <https://doi.org/10.1038/ngeo2028>
- Ding W, Yan Z, Wang J, Zhang J, Zhu D, Sun T, Wang S, He C, Shen R (1992) Geological report of the Xiaolinggen Au deposit. In: The thirteen geological team. Hebei Bureau of Geology and Mineral Resources, p 101
- Dong Y, Zhang G, Neubauer F, Liu X, Genser J, Hauenberger C (2011) Tectonic evolution of the Qinling orogen, China: review and synthesis. *J Asian Earth Sci* 41(3):213–237. <https://doi.org/10.1016/j.jseaes.2011.03.002>
- Du J, Audétat A (2020) Early sulfide saturation is not detrimental to porphyry Cu–Au formation. *Geology* 48(5):519–524. <https://doi.org/10.1130/G47169.1>
- Foden JD, Green DH (1992) Possible role of amphibole in the origin of andesite: some experimental and natural evidence. *Contrib Mineral Petr* 109(4):479–493. <https://doi.org/10.1007/BF00306551>
- Fortin M, Riddle J, Desjardins-Langlais Y, Baker DR (2015) The effect of water on the sulfur concentration at sulfide saturation (SCSS) in natural melts. *Geochim Cosmochim Acta* 160:100–116. <https://doi.org/10.1016/j.gca.2015.03.022>
- Griffin WL, Begg GC, O'Reilly SY (2013) Continental-root control on the genesis of magmatic ore deposits. *Nat Geosci* 6(11):905–910. <https://doi.org/10.1038/ngeo1954>
- Groves DI, Goldfarb RJ, Gebre-Mariam M, Hagemann SG, Robert F (1998) Orogenic gold deposits: a proposed classification in the context of their crustal distribution and relationship to other gold deposit types. *Ore Geol Rev* 13(1–5):7–27. [https://doi.org/10.1016/S0169-1368\(97\)00012-7](https://doi.org/10.1016/S0169-1368(97)00012-7)
- Holloway JR, Burnham CW (1972) Melting relations of basalt with equilibrium water pressure less than total pressure. *J Petrol* 13(1):1–29. <https://doi.org/10.1093/ptrology/13.1.1>
- Hou Z, Zhou Y, Wang R, Zheng Y, He W, Zhao M, Evans NJ, Weinberg RF (2017) Recycling of metal-fertilized lower continental crust: origin of non-arc Au-rich porphyry deposits at cratonic edges. *Geology* 45(6):563–566. <https://doi.org/10.1130/G38619.1>
- Jenner FE, O'Neill HSC (2012) Analysis of 60 elements in 616 ocean floor basaltic glasses. *Geochem Geophys Geosyst* 13(2). <https://doi.org/10.1029/2011GC003890>
- Jensen EP, Barton MD (2000) Gold deposits related to alkaline magmatism. *SEG Spec Publ* 13(13):279–314. <https://doi.org/10.1007/s00126-001-0226-7>
- Jugo PJ, Wilke M, Botcharnikov RE (2010) Sulfur K-edge XANES analysis of natural and synthetic basaltic glasses: implications for S speciation and S content as function of oxygen fugacity. *Geochim Cosmochim Acta* 74(20):5926–5938. <https://doi.org/10.1016/j.gca.2010.07.022>
- Kouzmanov K, Pokrovski GS (2012) Hydrothermal controls on metal distribution in porphyry Cu (–Mo–Au) systems. *SEG Spec Publ* 16:573–618. <https://doi.org/10.5382/SP.16.22>
- Kullerud G, Yund A, Moh GH (1969) Phase relations in the Cu–Fe–S, Cu–Ni–S and Fe–Ni–S systems. *Econ Geol Monogr* 4:323–343. <https://doi.org/10.5382/Mono.04.23>
- Lee CA, Luffi P, Chin EJ, Bouchet R, Dasgupta R, Morton DM, Le Roux V, Yin Q, Jin D (2012) Copper systematics in arc magmas and implications for crust–mantle differentiation. *Science* 336(6077):64–68. <https://doi.org/10.1126/science.1217313>
- Li Y, Audétat A (2012) Partitioning of V, Mn Co, Ni, Cu, Zn, As, Mo, Ag, Sn, Sb, W, Au, Pb, and Bi between sulfide phases and hydrous basanite melt at upper mantle conditions. *Earth Planet Sci Lett* 355:327–340. <https://doi.org/10.1016/j.epsl.2012.08.008>
- Li Y, Audétat A (2015) Effects of temperature, silicate melt composition, and oxygen fugacity on the partitioning of V, Mn Co, Ni, Cu, Zn, As, Mo, Ag, Sn, Sb, W, Au, Pb, and Bi between sulfide phases and silicate melt. *Geochim Cosmochim Acta* 162:25–45. <https://doi.org/10.1016/j.gca.2015.04.036>
- Li C, Barnes S, Makovicky E, Rose-Hansen J, Makovicky M (1996) Partitioning of nickel, copper, iridium, rhenium, platinum, and palladium between monosulfide solid solution and sulfide liquid: effects of composition and temperature. *Geochim Cosmochim Acta* 60(7):1231–1238. [https://doi.org/10.1016/0016-7037\(96\)00009-9](https://doi.org/10.1016/0016-7037(96)00009-9)
- Li J, Bi S, Selby D, Chen L, Vasconcelos P, Thiede D, Zhou M, Zhao X, Li Z, Qiu H (2012) Giant Mesozoic gold provinces related to the destruction of the North China craton. *Earth Planet Sci Lett* 349:26–37. <https://doi.org/10.1016/j.epsl.2012.06.058>
- Li Y, Feng L, Kiseeva ES, Gao Z, Guo H, Du Z, Wang F, Shi L (2019) An essential role for sulfur in sulfide–silicate melt partitioning of gold and magmatic gold transport at subduction settings. *Earth Planet Sci Lett* 528:115850. <https://doi.org/10.1016/j.epsl.2019.115850>
- Liu Y, Brenan J (2015) Partitioning of platinum-group elements (PGE) and chalcogens (Se, Te, As, Sb, Bi) between monosulfide–solid solution (MSS), intermediate solid solution (ISS) and sulfide liquid at controlled  $f_{O_2}$ – $f_{S_2}$  conditions. *Geochim Cosmochim Acta* 159:139–161. <https://doi.org/10.1016/j.gca.2015.03.021>
- Liu Y, Gao S, Gao C, Zong K, Hu Z, Ling W (2010) Garnet-rich granulite xenoliths from the Hannuoba basalts, North China: petrogenesis and implications for the Mesozoic crust–mantle interaction. *J Earth Sci China* 21(5):669–691. <https://doi.org/10.1007/s12583-010-0125-x>
- Lowenstern JB (2001) Carbon dioxide in magmas and implications for hydrothermal systems. *Miner Deposit* 36(6):490–502. <https://doi.org/10.1007/s001260100185>
- Matjuschkin V, Blundy JD, Brooker RA (2016) The effect of pressure on sulphur speciation in mid-to deep-crustal arc magmas and implications for the formation of porphyry copper

- deposits. *Contrib Miner Petrol* 171(7):66. <https://doi.org/10.1007/s00410-016-1274-4>
- Melekhova E, Blundy J, Robertson R, Humphreys MC (2015) Experimental evidence for polybaric differentiation of primitive arc basalt beneath St. Vincent lesser Antilles. *J Petrol* 56(1):161–192. <https://doi.org/10.1093/ptrology/egu074>
- Mungall JE, Brenan JM (2014) Partitioning of platinum-group elements and Au between sulfide liquid and basalt and the origins of mantle-crust fractionation of the chalcophile elements. *Geochim Cosmochim Acta* 125:265–289. <https://doi.org/10.1016/j.gca.2013.10.002>
- Muntean JL, Cline JS, Simon AC, Longo AA (2011) Magmatic-hydrothermal origin of Nevada's Carlin-type gold deposits. *Nat Geosci* 4(2):122–127. <https://doi.org/10.1038/ngeo1064>
- Qu K (2012) Geology and mineralization in Mujicun porphyry Cu–Mo deposit, northern Taihang Mt. China. China University of Geosciences, Beijing, p 78
- Richards JP (2009) Postsubduction porphyry Cu–Au and epithermal Au deposits: products of remelting of subduction-modified lithosphere. *Geology* 37(3):247–250. <https://doi.org/10.1130/G25451A.1>
- Richards JP, Kerrich R (2007) Special paper: adakite-like rocks: their diverse origins and questionable role in metallogenesis. *Econ Geol* 102(4):537–576. <https://doi.org/10.2113/gsecongeo.102.4.537>
- Rottier B, Audétat A (2019) In-situ quantification of chlorine and sulfur in glasses, minerals and melt inclusions by LA-ICP-MS. *Chem Geol* 504:1–13. <https://doi.org/10.1016/j.chemgeo.2018.11.012>
- Shi JL, Fang LM, Wang QC, Liu TC, Zhang SQ, Chen SK, Bi ZW (1980) Report for Regional Geological and Mineral Survey of People's Republic of China: Dongtuanbao (J-50-14-B), Wanganzhen (J-50-14-D), and Zijinguan (J-50-15-C) 1:50000. In: The first Regional Geological Survey Team, Hebei Bureau of Geology, p 219
- Sillitoe RH (2010) Porphyry copper systems. *Econ Geol* 105(1):3–41. <https://doi.org/10.2113/gsecongeo.105.1.3>
- Sillitoe RH (2018) Why no porphyry copper deposits in Japan and South Korea? *Resour Geol* 68(2):107–125. <https://doi.org/10.1111/rge.12156>
- Tan J, Wei J, Audétat A, Pettke T (2012) Source of metals in the Guocheng gold deposit, Jiaodong Peninsula, North China Craton: link to early Cretaceous mafic magmatism originating from Paleoproterozoic metasomatized lithospheric mantle. *Ore Geol Rev* 48:70–87. <https://doi.org/10.1016/j.oregeorev.2012.02.008>
- Tang L, Santosh M (2018) Neoproterozoic–Paleoproterozoic terrane assembly and Wilson cycle in the North China Craton: an overview from the central segment of the Trans-North China Orogen. *Earth Sci Rev* 182:1–27. <https://doi.org/10.1016/j.earscirev.2018.04.010>
- Tassara S, González-Jiménez JM, Reich M, Schilling ME, Morata D, Begg G, Saunders E, Griffin WL, O'Reilly SY, Grégoire M (2017) Plume-subduction interaction forms large auriferous provinces. *Nat Commun* 8(1):843. <https://doi.org/10.1038/s41467-017-00821-z>
- Ulmer P, Kaegi R, Müntener O (2018) Experimentally derived intermediate to silica-rich arc magmas by fractional and equilibrium crystallization at 1.0 GPa: an evaluation of phase relationships, compositions, liquid lines of descent and oxygen fugacity. *J Petrol* 59(1):11–58. <https://doi.org/10.1093/ptrology/egy017>
- Wallace PJ (2005) Volatiles in subduction zone magmas: concentrations and fluxes based on melt inclusion and volcanic gas data. *J Volcanol Geoth Res* 140(1–3):217–240. <https://doi.org/10.1016/j.jvolgeores.2004.07.023>
- Wang H, Mo X (1995) An outline of the tectonic evolution of China. *Episodes* 18:6–16. <https://doi.org/10.18814/epiugs/1995/v18i1.2/003>
- Wang S, Hu J, Song Y, Cai X, Wang T (2015) Stable isotopic geochemical and geochronological constraints on the formation of the Shihu gold deposit: the intracontinental metallogeny of the Taihang tectonic belt, eastern China. *Resour Geol* 65(3):249–265. <https://doi.org/10.1111/rge.12069>
- Wang Z, Cheng H, Zong K, Geng X, Liu Y, Yang J, Wu F, Becker H, Foley S, Wang CY (2020a) Metasomatized lithospheric mantle for Mesozoic giant gold deposits in the North China craton. *Geology* 48(2):169–173. <https://doi.org/10.1130/G46662.1>
- Wang Z, Wang X, Cheng H, Ma L, Cai Y, Foley S, Xiong L (2020b) Gold and PGE contents of lamprophyres in Jiaodong Peninsula: insights into metal enrichment and release from the metasomatized mantle source for giant gold deposits. *Goldschmidt2020 Abstract*
- Wones DR (1989) Significance of the assemblage titanite + magnetite + quartz in granitic rocks. *Am Miner* 74(7–8):744–749
- Wu F, Yang J, Xu Y, Wilde SA, Walker RJ (2019) Destruction of the North China craton in the Mesozoic. *Annu Rev Earth Planet Sci* 47:173–195. <https://doi.org/10.1146/annurev-earth-053018-060342>
- Xiao W, Windley BF, Hao J, Zhai M (2003) Accretion leading to collision and the Permian Solonker suture, Inner Mongolia, China: termination of the central Asian orogenic belt. *Tectonics* 22(6):1–21. <https://doi.org/10.1029/2002TC001484>
- Yang J, Wu F, Wilde SA (2003) A review of the geodynamic setting of large-scale Late Mesozoic gold mineralization in the North China Craton: an association with lithospheric thinning. *Ore Geol Rev* 23(3–4):125–152. [https://doi.org/10.1016/S0169-1368\(03\)00033-7](https://doi.org/10.1016/S0169-1368(03)00033-7)
- Yang Z, Cooke DR (2020) Porphyry copper deposits in China. *SEG Spec Publ* 22(22):133–188. <https://doi.org/10.5382/SP.22.05>
- Zajacz Z, Seo JH, Candela PA, Piccoli PM, Heinrich CA, Guillon M (2010) Alkali metals control the release of gold from volatile-rich magmas. *Earth Planet Sci Lett* 297(1–2):50–56. <https://doi.org/10.1016/j.epsl.2010.06.002>
- Zhang D, Audétat A (2017) What caused the formation of the giant Bingham Canyon porphyry Cu–Mo–Au deposit? Insights from melt inclusions and magmatic sulfides. *Econ Geol* 112(2):221–244. <https://doi.org/10.2113/econgeo.112.2.221>
- Zhang S, Zhao Y, Davis GA, Ye H, Wu F (2014) Temporal and spatial variations of Mesozoic magmatism and deformation in the North China Craton: implications for lithospheric thinning and decratonization. *Earth Sci Rev* 131:49–87. <https://doi.org/10.1016/j.earscirev.2013.12.004>
- Zhang J, Li S, Santosh M, Niu S, Li Q, Lu J (2017) The magmatic-hydrothermal mineralization systems of the Yixingzhai and Xinzhuang gold deposits in the central North China Craton. *Ore Geol Rev* 88:416–435. <https://doi.org/10.1016/j.oregeorev.2017.05.030>
- Zhang L, Weinberg RF, Yang L, Groves DI, Sai S, Matchan E, Phillips D, Kohn BP, Miggins DP, Liu Y (2020) Mesozoic orogenic gold mineralization in the Jiaodong Peninsula, China: a focused event at 120±2 Ma during cooling of pregold granite intrusions. *Econ Geol* 115(2):415–441. <https://doi.org/10.5382/econgeo.4716>
- Zhao G, Sun M, Wilde SA, Sanzhong L (2005) Late Archean to Paleoproterozoic evolution of the North China Craton: key issues revisited. *Precambrian Res* 136(2):177–202. <https://doi.org/10.1016/j.precambres.2004.10.002>
- Zheng T, Duan Y, Xu W, Ai Y, Chen L, Zhao L, Zhang Y, Xu X (2016) Crust and upper mantle velocity model of North China v2.4. <http://www.craton.cn/data>
- Zhu G, Niu M, Xie C, Wang Y (2010) Sinistral to normal faulting along the Tan-Lu Fault Zone: Evidence for geodynamic switching of the East China continental margin. *J Geol* 118(3):277–293. <https://doi.org/10.1086/651540>

- Zhu R, Chen L, Wu F, Liu J (2011) Timing, scale and mechanism of the destruction of the North China Craton. *Sci China Earth Sci* 54(6):789–797. <https://doi.org/10.1007/s11430-011-4203-4>
- Zhu R, Yang J, Wu F (2012) Timing of destruction of the North China Craton. *Lithos* 149:51–60. <https://doi.org/10.1016/j.lithos.2012.05.013>
- Zhu R, Fan H, Li J, Meng Q, Li S, Zeng Q (2015) Decratonic gold deposits. *Sci China Earth Sci* 58(9):1523–1537. <https://doi.org/10.1007/s11430-015-5139-x>
- Zhu R, Zhu G, Li J (2019) Destruction of the North China Craton. Science Publishing House, Beijing, pp 296–304
- Publisher's Note** Springer Nature remains neutral with regard to jurisdictional claims in published maps and institutional affiliations.